

Effects of shear methods on shear strengths and deformation modes of two typical transition metal carbides and their unification

Chuanying Li ¹, Tao Fu ^{1,2,*}, Xule Li¹, Hao Hu ¹ and Xianghe Peng ^{1,2,*}

¹Department of Engineering Mechanics, Chongqing University, Chongqing 400044, China

²State Key Laboratory of Coal Mine Disaster Dynamics and Control, Chongqing University, Chongqing 400044, China



(Received 15 September 2022; revised 9 May 2023; accepted 13 June 2023; published 21 June 2023)

Simple shear and pure shear are two common methods for investigating the mechanical responses of materials using first-principles calculations; however, the stress-strain responses and deformation modes obtained are different. Taking HfC and TaC as examples, we first investigated their mechanical responses under the two methods, then proposed a semiconstrained method that combines the advantages of the two methods and can better describe their mechanical responses. Furthermore, we extended the Mohr-Coulomb relation to unify the shear stresses obtained in different ways, which can explain the enhancement of yield shear strength caused by pressure in terms of the friction between atomic layers.

DOI: [10.1103/PhysRevB.107.224106](https://doi.org/10.1103/PhysRevB.107.224106)

I. INTRODUCTION

Calibrating the theoretical strengths and revealing the deformation modes of existing hard materials are the foundation for developing new superhard materials [1]. Theoretical strength and ductility are generally associated with bond strength, crystalline symmetry, and deformation mode [2]. The group IVB and VB transition metal carbides (TMCs) provide a perfect test platform to explore the effect of subtle differences in bonding on mechanical responses [3]. They possess a rocksalt structure with mixed bonding (covalent, metallic, and ionic) characteristics, resulting in high hardness, and good thermal and electrical conductivity [4,5]. However, group IVB TMCs and group VB TMCs exhibit different deformation modes: the easiest slip system in the former is $\langle 110 \rangle \{110\}$, while that in the latter is $\langle 110 \rangle \{111\}$ [3,6–9]. Furthermore, the practical slip behavior of TMCs is sensitive to testing conditions; for instance, slip on $\langle 110 \rangle \{001\}$ was observed for ZrC [10], while mixed slip on the $\{110\}$ and $\{111\}$ planes occurred in NbC tested at room temperature [11]. Moreover, micronanomechanical experiments combined with advanced microstructure characterization can provide powerful means to explore the deformation mode, but they have high requirements for sample quality and experimental equipment. Therefore, atomic-scale numerical calculations, including first-principles calculation (FPC) and molecular dynamics (MD) simulation, have been widely used to calibrate the theoretical strength and explore the deformation mode of materials. Limited by the accuracy of interatomic potentials used in MD simulation, materials with complex bonding

characteristics, such as carbides, nitrides, and diamonds, are studied mainly using FPC [12–14].

Simple shear and pure shear are two common methods for investigating the mechanical responses and microstructural evolutions of materials using FPC. Frenkel [15] confined the shear to the displacement between two adjacent atomic planes; then some other researchers permitted uniform shear but constrained the deformation to be rigid in the shear plane [16–18], called simple shear (SS). These constraints are considered unreasonable and always lead to overestimating shear strength [19,20]. Subsequently, Morris and co-workers proposed a method that allows the structural relaxation of all other five strain components except the applied shear strain component [21,22], called pure shear (PS), which makes shear strength reduced by 35%–45% compared with that under SS [21]. The schematics of PS and SS are illustrated in Figs. 1(a) and 1(b). The temperature effect was considered in *ab initio* molecular dynamics (AIMD) under the canonical (*NVT*) ensemble, which leads to much lower theoretical strength than that at $T = 0$ K [23–25]. However, controlling P and T during shear simulations by AIMD under the isothermal-isobaric (*NPT*) ensemble is still challenging [26,27]. Therefore, AIMD simulation for shear usually uses the *NVT* ensemble. It is also challenging to analyze the effect of temperature-induced normal pressure on shear stress under the condition of constant volume, compared with that obtained using the *NPT* ensemble. In FPC, PS and SS correspond, respectively, to the *NPT* and *NVT* ensembles at $T = 0$ K, where a marked difference exists between the shear stresses (or the normal stresses) [21], though there is no temperature-induced volume change. Therefore, investigating the effects of constant volume could help to explain why SS overestimates yield shear strength in FPC.

Besides, in FPC for diamond, PS leads to a graphitized structure due to instability [28–30]. However, dislocation-mediated plastic deformation of diamond is observed at room temperature [31]. Therefore, appropriate boundary

*Present address: Department of Engineering Mechanics, Chongqing University, Chongqing 400044, China.

[†]futao@cqu.edu.cn

[‡]xhpeng@cqu.edu.cn

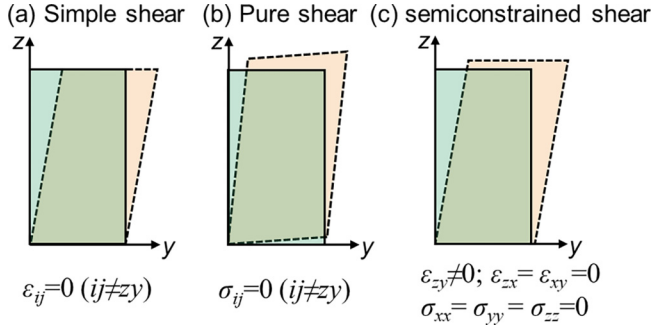


FIG. 1. Schematics of (a) simple shear, (b) pure shear, and (c) semiconstrained shear.

conditions should be developed for more realistic simulations for shear. The same material may exhibit different failure mechanisms under various loading conditions [32]. Furthermore, the Mohr-Coulomb relation is used to describe the dependence of the yield shear strength of brittle materials on the stress component normal to the shear displacement [33,34], which may help to unify the yield shear strengths obtained under different loading conditions (e.g., SS and PS).

In this work, taking HfC and TaC as examples, we first investigate their mechanical responses under PS and SS using FPC, and build the connections between the yield shear strengths obtained by PS and SS using the Mohr-Coulomb relation. Through analyzing the advantages and disadvantages of the two methods, a semiconstrained method is proposed to study the mechanical responses of HfC and TaC. Our study illustrates the connection between the deformation modes of HfC and TaC sheared with different methods and unifies their shear stresses by the Mohr-Coulomb relation.

II. METHOD

We investigate the mechanical responses of HfC and TaC under PS and SS, respectively, by the applied $\Delta\epsilon_{zy} = 0.01$ to determine the shear stress σ_{zy} . During deformation, the lattice vectors need to be changed, while the fractional coordinates of the atomic positions stay unchanged, causing the supercell shape and atomic Cartesian coordinates to change accordingly [35]. Hence, the deformation can be imposed by transforming the i -th step lattice vector matrix \mathbf{R}^{i-1} to the deformed i th step lattice vector matrix \mathbf{R}^i as follows [36]:

$$\mathbf{R}^i = \mathbf{R}^{i-1} \left[\mathbf{I} + \begin{pmatrix} 0 & 0 & 0 \\ 0 & 0 & 0 \\ 0 & \Delta\epsilon_{zy} & 0 \end{pmatrix} \right].$$

For PS, after each $\Delta\epsilon_{zy}$, the atomic coordinates and the other five independent strain components (except ϵ_{zy}) are optimized simultaneously to reach a stress state with $\sigma_{xx} = \sigma_{yy} = \sigma_{zz} = \sigma_{xy} = \sigma_{zx} = 0$ [35,37,38]. For SS, after applying $\Delta\epsilon_{zy}$, the atomic coordinates are optimized but remain $\epsilon_{xx} = \epsilon_{yy} = \epsilon_{zz} = \epsilon_{xy} = \epsilon_{zx} = 0$ [14,39]. The schematics of PS and SS are illustrated in Figs. 1(a) and 1(b), respectively. During optimization, the projected-augmented waves (PAW) [40] with the Perdew-Burke-Ernzerhof (PBE) [41] form of exchange-correlation potentials are adopted [42]. The plane-wave cutoff energy is set to 550 eV. Monkhorst Pack k -mesh grids with

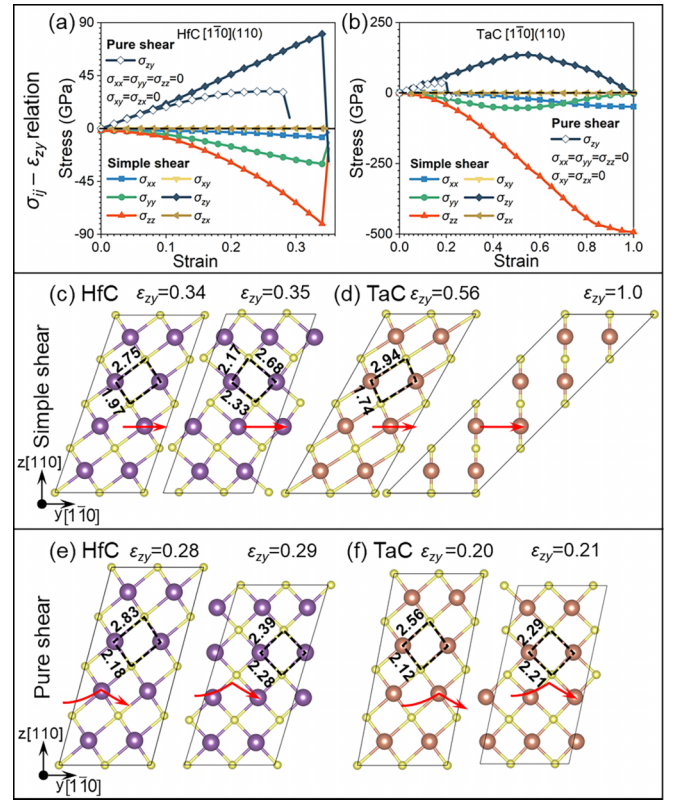


FIG. 2. Mechanical response of samples sheared along $[1\bar{1}0](110)$. (a), (b) Variations of stress components of HfC and TaC with ϵ_{zy} under SS and PS, respectively. Atomic distributions of (c) HfC and (d) TaC under SS; (e) HfC and (f) TaC under PS. Red curves are atomic motion trajectories.

2000 k points per reciprocal atom are used in both HfC and TaC. The electronic energy and the ionic force convergence criteria are 10^{-5} eV/supercell and 0.01 eV/Å, respectively. Experiments showed that the potential slip systems of the TMCs are $\{110\}\{110\}$, $\{110\}\{111\}$, and $\{112\}\{111\}$, so the corresponding crystallographic orientation relations are $x \parallel [001]$, $y \parallel [1\bar{1}0]$, and $z \parallel [110]$; $x \parallel [\bar{1}\bar{1}2]$, $y \parallel [1\bar{1}0]$, and $z \parallel [111]$; and $x \parallel [1\bar{1}0]$, $y \parallel [\bar{1}\bar{1}2]$, and $z \parallel [111]$, respectively. All the first-principles calculations are performed with the Vienna *ab initio* simulation package (VASP) [42,43].

III. RESULTS AND DISCUSSION

A. Mechanical responses under simple shear and pure shear

We first investigate the mechanical responses of HfC and TaC under SS and PS along $[1\bar{1}0](110)$, as shown in Fig. 2. The $\{001\}$ atomic planes of HfC and TaC are cut open to analyze the deformation modes. Before loading, the initial bond lengths of HfC and TaC are 2.32 and 2.24 Å, respectively (Fig. SI in the Supplemental Material [44]), which are half of their lattice constants. Figures 2(a) and 2(b) show the variations of stress components σ_{ij} with ϵ_{zy} of HfC and TaC, respectively. With the increase of ϵ_{zy} , σ_{zy} increases to its peak and then decreases (corresponding to yield behavior). Meanwhile, the other five stress components are kept at zero under PS, but

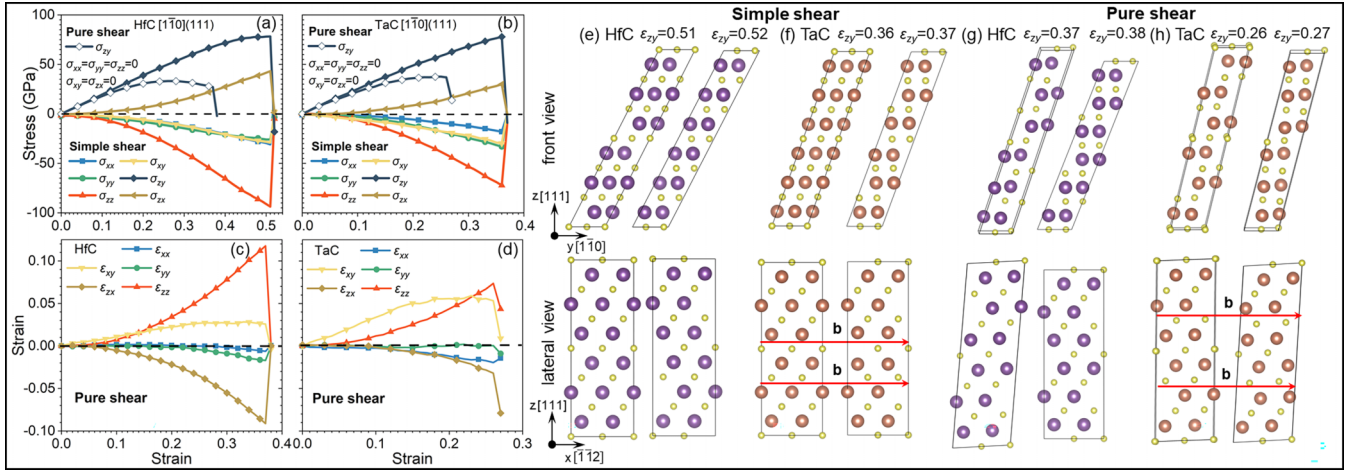


FIG. 3. Mechanical responses of samples sheared along $[1\bar{1}0](111)$. Variation of stress components in (a) HfC and (b) TaC with ε_{zy} under SS and PS, and variations of strain components in (c) HfC and (d) TaC with ε_{zy} under PS. Front (upper) and lateral (lower) views of atomic distributions: (e) HfC and (f) TaC under SS; (g) HfC; and (h) TaC under PS. The Burger's vector $\mathbf{b} = 1/6[\bar{1}\bar{1}2]a$.

some may increase under SS. In particular, $|\sigma_{zz}|$ increases sharply under SS, even more than σ_{zy} . The red curves in Figs. 2(c)–2(f) show the atomic motion trajectories, where the atoms are located at different positions on the trajectory at different strains.

For HfC (TaC) under SS, the atoms move horizontally as ε_{zy} increases, resulting in half of the Hf-C (Ta-C) bonds in the $\{001\}$ plane being stretched to 2.75 Å (2.94 Å) while the others are compressed to 1.97 Å [Fig. 2(c) at $\varepsilon_{zy} = 0.34$] (1.74 Å [Fig. 2(d) at $\varepsilon_{zy} = 0.56$]). After yield and a new equilibrium state is reached in HfC, the Hf-C bonds in the $\{001\}$ plane show three different lengths (2.17, 2.33, and 2.68 Å) [Fig. 2(c) at $\varepsilon_{zy} = 0.35$], which would alleviate the enormous energy caused by the shortening of the Hf-C bonds and reduce the other stress components [Fig. 2(a)]. While in TaC, half of the Ta-C bonds in the $\{001\}$ plane continue to be compressed, and the others continue to be stretched. There is no apparent structural failure and σ_{zy} does not “drop” suddenly [Figs. 2(b) and 2(d)]. At $\varepsilon_{zy} = 1.0$, σ_{zy} tends to zero, as shown in Fig. 2(b). However, $|\sigma_{zz}|$ increases persistently and surpasses σ_{zy} , attributed to the supercell being unrelaxed in the z direction so that atoms would be too close and the repulsion would be increased remarkably.

For PS, due to the full relaxation of σ_{xx} , σ_{yy} , σ_{zz} , σ_{xy} , and σ_{zx} , the supercells would expand in the z direction to avoid the atoms getting too close, and the trajectories show that the atoms move upwards during shear deformation [Fig. 2(e) at $\varepsilon_{zy} = 0.28$, and Fig. 2(f) at $\varepsilon_{zy} = 0.20$]. Atoms always remain in relatively low-energy positions, and the variation of bond length is within an acceptable range. HfC and TaC exhibit the same deformation mode related to the perfect slip along $[1\bar{1}0](110)$. After yield, the bond lengths are close to the initial ones, and the atomic trajectories show how the atoms complete energy barrier transitions [Figs. 2(e) and 2(f)]. HfC and TaC revert to their initial states after a slip by $a/2[1\bar{1}0]$, which is different from that under SS, where the atoms cannot cross the energy barrier to reach their initial states and σ_{zy} of TaC does not “drop” suddenly, and the supercells yield, as shown in Figs. 2(c) and 2(d).

Figures 3(a) and 3(b) show the variations of σ_{ij} with ε_{zy} under shear along $[1\bar{1}0](111)$. Like that along $[1\bar{1}0](110)$, σ_{zy} under SS is larger than that under PS. Figures 3(c) and 3(d) show the variations of the other five strain components with ε_{zy} under PS. In the front and lateral views [Fig. 3(e) at $\varepsilon_{zy} = 0.52$ under SS, and Fig. 3(g) at $\varepsilon_{zy} = 0.38$ under PS], HfC exhibits a uniform yield mode, and the atomic distributions after yield are similar to that at $\varepsilon_{zy} = 0$ (Fig. SII in the Supplemental Material [44]). However, in the lateral view of TaC at $\varepsilon_{zy} = 0.37$ under SS [Fig. 3(f)] and $\varepsilon_{zy} = 0.27$ under PS [Fig. 3(h)], a partial slip along $[\bar{1}\bar{1}2]$ occurs, although the shear is applied along $[1\bar{1}0]$, indicating that the slip along $[\bar{1}\bar{1}2]$ occurs prior to that along $[1\bar{1}0]$.

Previous experimental results showed that $\langle 110 \rangle \{110\}$ is the easiest slip system in HfC, while $\langle 110 \rangle \{111\}$ slip is observed in TaC at room temperature [8,9,45,46], which is constituted by two partial dislocations and a stacking fault ($\frac{a}{2}[10\bar{1}] \rightarrow \frac{a}{6}[11\bar{2}] + \text{ISF} + \frac{a}{6}[2\bar{1}\bar{1}]$) [47,48]. Therefore, intrinsic stacking fault (ISF) energy γ_{isf} is often used to indicate the dislocation dissociation ability in TMCs [49]. The lower γ_{isf} of TaC obtained by FPC confirms its dissociation ability, which is absent in HfC due to its higher γ_{isf} [3,6]. It can account for why, as the shear strain is applied along $[1\bar{1}0]$, slip would occur along $[1\bar{1}0]$ in HfC for $a/2[1\bar{1}0]$, while in TaC, slip occurs along $[\bar{1}\bar{1}2]$. Moreover, for PS, the supercell would be distorted during deformation; ε_{xy} and ε_{zx} increase obviously with ε_{zy} [Figs. 3(c) and 3(d)]. Although, after yield, $\varepsilon_{xy} = \varepsilon_{zx} = 0$ at $\varepsilon_{zy} = 0.38$ in HfC [Fig. 3(g)], ε_{zx} in TaC is still non-negligible [Fig. 3(h) at $\varepsilon_{zy} = 0.27$]. This distortion leads to a slight change in the direction of the applied strain, which is no longer the initial $[1\bar{1}0]$ direction, causing the release of a part of the stress and unreal σ_{zy} .

Similar to the above two situations, the maximum value of σ_{zy} under SS is much larger than that under PS along $[\bar{1}\bar{1}2](111)$ (Figs. SIII(a) and SIII(b) [44]). The deformation modes of HfC and TaC are the partial slip along $[\bar{1}\bar{1}2](111)$, indicating that, in this case, the shear methods have an insignificant effect on the deformation modes (Figs. SIII(c)–SIII(f) [44]).

B. Extension of the Mohr-Coulomb relation

The above analyses for the mechanical responses of HfC and TaC under PS and SS show that σ_{zy} under SS is much larger than that under PS because $\varepsilon_{zz} = 0$. Hence, the atoms in the z direction under SS are more compact than those under PS, resulting in larger repulsive force and atomistic friction, equivalent to applying pressure in the z direction. Based on friction law, we notice that the Mohr-Coulomb criterion can consider the effect of normal stress on shear stress by [33,34]

$$\sigma_{zy} = \sigma_{zy0} - \alpha\sigma_{zz}, \quad (1)$$

where σ_{zy} and σ_{zy0} are the yield shear stress under the normal stress σ_{zz} (compressive stress, negative value) and that under $\sigma_{zz} = 0$, respectively; α , which is non-negative, is a system-specific coefficient related to the internal frictional property. In this work, we extend this macroscopic relation to building the connection between shear stress and normal stress during deformation,

$$\sigma_{zy}(\varepsilon) = \sigma_{zy0}(\varepsilon) - \alpha\sigma_{zz}(\varepsilon), \quad (2)$$

where $\sigma_{zy}(\varepsilon)$ and $\sigma_{zy0}(\varepsilon)$ are shear stresses at ε with normal stress $\sigma_{zz}(\varepsilon)$ and $\sigma_{zz} = 0$, respectively.

Next, we utilize Eq. (2) to build the connection between the shear stress under PS and that under SS. Letting the yield shear stress under PS in Eq. (1) be σ_{zy0} , and the shear stress and normal stress at the corresponding strain under SS be σ_{zy} and σ_{zz} , respectively, α can be determined by $\alpha = -(\sigma_{zy} - \sigma_{zy0})/\sigma_{zz}$. Then, $\sigma_{zy}(\varepsilon)$ under SS [$\sigma_{zz}(\varepsilon) \neq 0$] can be converted to $\sigma_{zy0}(\varepsilon)$ ($\sigma_{zz} = 0$) by

$$\sigma_{zy0}(\varepsilon) = \sigma_{zy}(\varepsilon) + \alpha\sigma_{zz}(\varepsilon). \quad (3)$$

Figures 4(a)–4(c) show that the $\sigma_{zy0}(\varepsilon)$ obtained by Eq. (3) is close to the σ_{zy} under PS, indicating that the Mohr-Coulomb relation can well describe the shear stress under PS and SS before yield. The Mohr-Coulomb relation could reasonably explain why the yield shear stress under SS is larger than that under PS, and describe the effect of pressure on the shear stress during deformation. Although the value of α varies along different crystallographic orientations, TaC and HfC exhibit close values of α for the same orientation, suggesting a correlation between α and crystallographic orientation, which will be further investigated in future work. Furthermore, α may vary with σ_{zz} ; however, in this work, we assume that it is a constant independent of σ_{zz} , which leads to a slight discrepancy between the curves before the peak stress. After the peak stress, the differences between the results obtained with the two methods become obvious along $[1\bar{1}0](111)$ [Fig. 4(b)], which may be ascribed to the distortion of the supercell under PS.

To avoid the unreasonable σ_{zz} under SS and abnormal distortion under PS, we suggest a semiconstrained shear (SCS) method, where the constraint of $\sigma_{xx} = \sigma_{yy} = \sigma_{zz} = 0$ and $\varepsilon_{xy} = \varepsilon_{yx} = 0$ is used. The schematic of SCS is illustrated in Fig. 1(c). Figures 4(d)–4(f) show the comparisons of the stresses along different directions converted using the Mohr-Coulomb relation under SS with those under SCS, where the differences after the peak stress decrease or even disappear, especially in the $[1\bar{1}0](111)$ direction [Fig. 4(e)], confirming

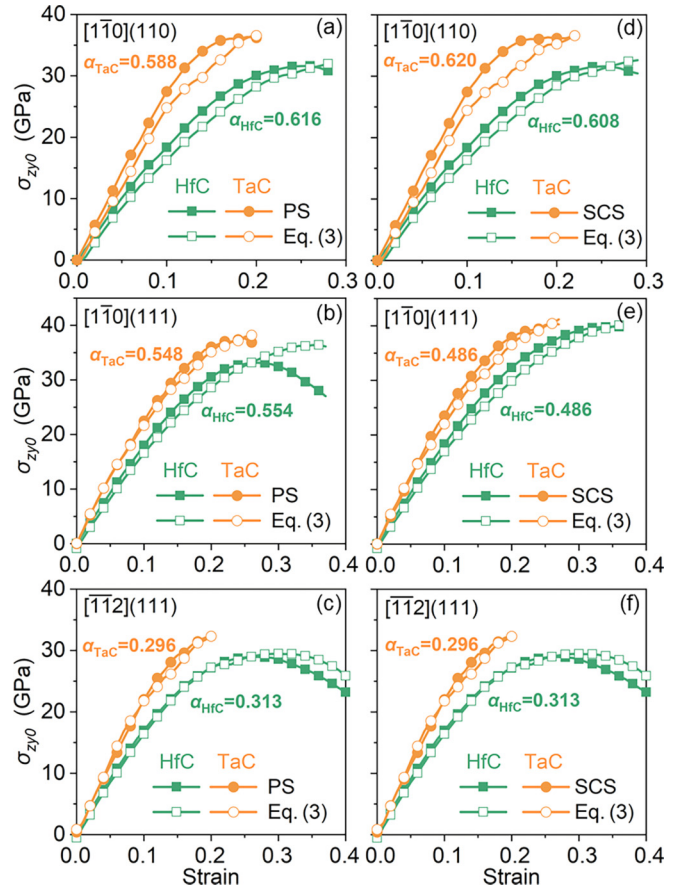


FIG. 4. Comparison of stresses along different directions converted using the Mohr-Coulomb relation under SS with those under (a)–(c) PS and under (d)–(f) SCS obtained by FPCs.

that the distortion of the supercell under PS significantly affects the stress state.

Considering that all atoms remain in zero-force high-symmetry positions because deformation under SS and PS occurs at 0 K without defects, this results in abnormally higher strengths than experiments, which may be difficult to avoid. Breaking this symmetry by a small displacement is an effective method [22]. Therefore, we introduce displacement perturbation at 0 K, which shows that it would reduce the yield stress and strain because it breaks the symmetry. However, the applicability of the Mohr-Coulomb relation during deformation between the normal stress and shear stress remains valid before yield. The α along the $[\bar{1}\bar{1}2](111)$ direction in the case with the perturbation is insignificantly different from that without the perturbation, as shown in Fig. 5. Furthermore, Fig. 6 shows that the stress-strain curves before yield are also close to each other, indicating that displacement perturbation has little effect on the deformation before yield. We only show results along $[\bar{1}\bar{1}2](111)$ because the results in this work indicate that deformation in the $[\bar{1}\bar{1}2](111)$ direction is less affected by the load methods, and the yield modes of HfC and TaC with displacement perturbation are also the partial slip along $[\bar{1}\bar{1}2](111)$. However, setting the size of the displacement perturbation is also a problem that needs careful consideration. If it is too large, it may directly skip the energy

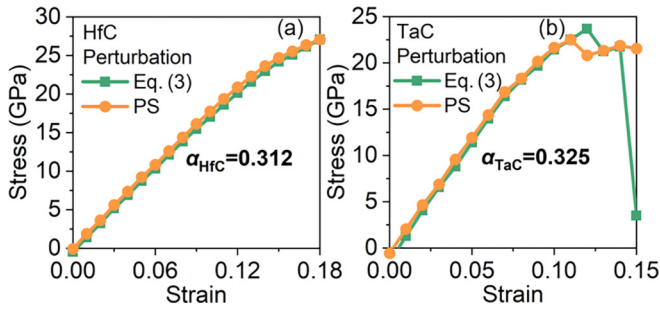


FIG. 5. Comparison of stresses of HfC and TaC along the $[\bar{1}\bar{1}2](111)$ direction converted by the Mohr-Coulomb relation under SS with that under PS, where displacement perturbations have been introduced.

instability point; if it is too small, it may fail to break the symmetry because the disturbed atoms may return to their highly symmetric positions. In this work, we use a series of different perturbations for shear simulation, but determining the most appropriate perturbation amplitude corresponding to an unstable phonon mode requires further investigation. It should be noted again that the perturbation mainly affects the yield critical point, thereby affecting the deformation mode, and the influence before yield can be ignored. Therefore, in our work, the Mohr-Coulomb relation is only used to describe the stress relation before yield.

By calculating the indentation strengths of superhard metallic compounds, diamond, boron nitride, and so on, Chen *et al.* noted that the deformation mode generated by the stress confinement during indentation is distinctly different from that under PS, and called this phenomenon strain stiffening [50–52]. Berkovich indentation shear (BIS) was calculated under a biaxial stress state that contains shear stress σ_{zx} and pressure σ_{zz} ($\sigma_{zz} = \sigma_{zx} \tan \Phi$, where $\Phi \sim 65^\circ$ or $\sim 68^\circ$

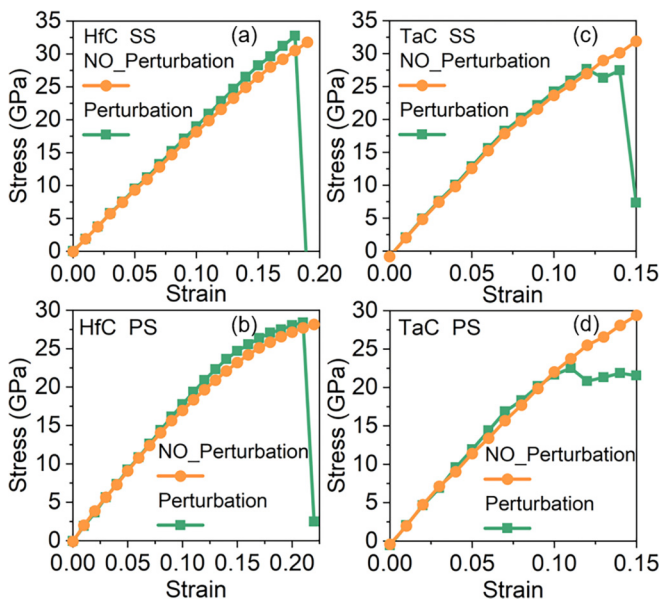


FIG. 6. Comparison between stress-strain curves under SS and PS of TaC and HfC sheared along the $[\bar{1}\bar{1}2](111)$ direction with or without displacement perturbation.

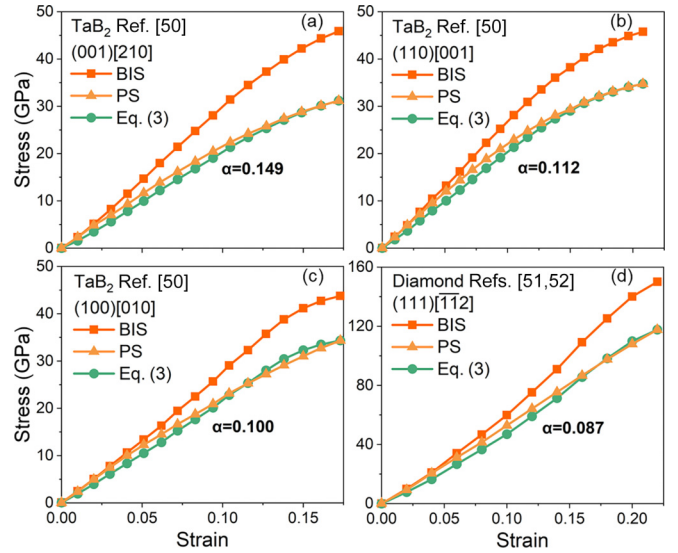


FIG. 7. Comparison of stresses converted by the Mohr-Coulomb relation under BIS with those under PS and BIS.

is the centerline to surface angle of the indenter) [50–52]. Using Eq. (3), we subtract the effect of the normal stress from the shear stresses obtained by the BIS, as shown in Fig. 7, and find that the Mohr-Coulomb relation can also well describe the connection of shear stresses under BIS and PS before failure, which delivers a reasonable explanation for the so-called strain stiffening phenomenon during an indentation in terms of the stress state. This so-called strain stiffening is essentially the result of an elevated frictional force due to compressive stress.

C. Mechanical responses under semiconstrained shear

Compared with the abnormal high shear stress under SS related to the shear-induced pressure in a constant volume, the supercell may tilt under PS [Figs. 3(g) and 3(h)] due to the full relaxation of σ_{xy} and σ_{zx} [Figs. 3(c) and 3(d)]. Combining the advantages of SS and PS and avoiding their disadvantages, a semiconstrained shear (SCS) is suggested, in which the distortion related to ε_{xy} and ε_{zx} can be avoided by keeping $\varepsilon_{xy} = \varepsilon_{zx} = 0$ while σ_{xx} , σ_{yy} , and σ_{zz} can be fully relaxed.

The σ_{zy} of HfC and TaC under SCS do not exhibit abnormally large values due to the relaxation in the z direction (the stress-strain curves are shown in Figs. SIV(a), SIV(d), and SIV(g) [44]). It can be seen in Figs. SIV(b) and SIV(c) that HfC and TaC exhibit the same deformation mode as that under PS along $[\bar{1}\bar{1}0](110)$, where the atomic trajectories show how the atoms cross the energy barrier. After yield, the bond lengths are close to the initial ones (Fig. SI). Figures SIV(e) and SIV(f) [44] show the atomic distributions along $[\bar{1}\bar{1}0](111)$ under SCS, where slip occurs along $[\bar{1}\bar{1}0]$ for $a/2$ $[\bar{1}\bar{1}0]$ in HfC, while slip occurs along $[\bar{1}\bar{1}2]$ in TaC despite shear deformation being applied along $[\bar{1}\bar{1}0](111)$. Meanwhile, the distortion of the supercell under PS can be avoided under SCS because $\varepsilon_{xy} = \varepsilon_{zx} = 0$, and the direction of the applied strain can stay unchanged. Figures SIV(h) and SIV(i) [44] show that the deformation modes of HfC and TaC are the partial slip along $[\bar{1}\bar{1}2](111)$ under SCS, similar to that under SS and PS.

TABLE I. Deformation modes (DMs) and yield strengths, σ_{zy}^{\max} (GPa), of HfC and TaC under SS, PS, and SCS along different directions. Calculated results of HfC and TaC reported in the literature are provided for comparison.

		HfC			TaC		
		[1 $\bar{1}$ 0](110)	[1 $\bar{1}$ 0](111)	[$\bar{1}$ 12](111)	[1 $\bar{1}$ 0](110)	[1 $\bar{1}$ 0](111)	[$\bar{1}$ 12](111)
SS	DM	Uniform failure	Perfect slip	Partial slip	Uniform failure	Partial slip	Partial slip
	σ_{zy}^{\max}	80.41	78.28	44.24	135.42	77.86	49.1
PS	DM	Perfect slip	Perfect slip	Partial slip	Perfect slip	Partial slip	Partial slip
	σ_{zy}^{\max}	31.6, 30 [22]	33.16, 34.5 [6]	28.97	36.35, 37.5 [53]	37.62, 37.4 [53]	32.31
SCS		Perfect slip	Perfect slip	Partial slip	Perfect slip	Partial slip	Partial slip
	σ_{zy}^{\max}	31.62	39.86	28.95	36.63	40.43	32.33

The yield strengths σ_{zy}^{\max} under SCS and PS are lower than that under SS, but close to each other except for the [1 $\bar{1}$ 0](111) direction, summarized in Table I, which includes the corresponding deformation modes. The results are consistent with the previous theoretical calculations in Refs. [6,22,53], demonstrating the reliability of our calculations. It should be noted that ε_{xx} , ε_{yy} , and ε_{zz} need not vanish because $\sigma_{xx} = \sigma_{yy} = \sigma_{zz} = 0$ under SCS, similar to the corresponding constraints under PS; however, ε_{xy} and ε_{zx} are kept at zero under SCS, which should be closer to actual shear deformation. The distortion of the supercell under PS along [1 $\bar{1}$ 0](111) in the xy and zx directions would reduce a part of the stress and result in a slight deviation from the prescribed shear direction, accounting for the lower σ_{zy}^{\max} under PS than that under SCS. Specifically speaking, compared with PS and SS, the SCS method can more reliably provide the actual stress and strain states, deformation mode, and microstructure evolution of supercells.

IV. CONCLUSIONS

In summary, we investigated the mechanical responses of HfC and TaC under pure shear and simple shear using first-principles calculations, respectively. The simple shear method

seriously overestimates the yield shear stress due to the internal friction induced by the normal stress and unrealistic deformation mode, while the pure shear method distorts the supercell, leading to a change in the loading direction. Considering the advantages and disadvantages of the two methods, a semiconstrained method was proposed to study the shear responses of HfC and TaC, which could better reflect the yield stress and deformation mode. Furthermore, the Mohr-Coulomb relation was used to unify the shear stresses obtained using different loading methods, which can also help to gain insight into the effect of pressure on shear stress, and provide a reasonable explanation for the strain stiffening during indentation in terms of stress state.

ACKNOWLEDGMENTS

This work was supported by the National Natural Science Foundation of China (Grants No. 12272066 and No. 11932004), Fundamental Research Funds for the Central Universities (Grant No. 2022CDJXY-012), and Chongqing Natural Science Foundation of Shanghai (Grants No. CSTB2022NSCQ-MSX0383 and No. CSTB2022NSCQ-BHX0704). We would like to express our gratitude to Dr. Georg Kresse for his valuable insights on the application of VASP.

-
- [1] N. Wang, Z. Fu, D. Legut, B. Wei, T. C. Germann, and R. Zhang, *Phys. Chem. Chem. Phys.* **21**, 16095 (2019).
 - [2] P. Paupler, *Cryst. Res. Technol.* **23**, 194 (1988).
 - [3] N. De Leon, X. X. Yu, H. Yu, C. R. Weinberger, and G. B. Thompson, *Phys. Rev. Lett.* **114**, 165502 (2015).
 - [4] W. S. Williams, *Prog. Solid State Chem.* **6**, 57 (1971).
 - [5] Y. Liu, Y. Jiang, R. Zhou, and J. Feng, *J. Alloys Compd.* **582**, 500 (2014).
 - [6] H. Yu, M. Bahadori, G. B. Thompson, and C. R. Weinberger, *J. Mater. Sci.* **52**, 6235 (2017).
 - [7] X.-X. Yu, C. R. Weinberger, and G. B. Thompson, *Comput. Mater. Sci.* **112**, 318 (2016).
 - [8] D. J. Rowcliffe and G. E. Hollox, *J. Mater. Sci.* **6**, 1261 (1971).
 - [9] S. Kiani, J.-M. Yang, and S. Kodambaka, *J. Am. Ceram. Soc.* **98**, 2313 (2015).
 - [10] S. Kiani, C. Ratsch, A. M. Minor, S. Kodambaka, and J. M. Yang, *Philos. Mag.* **95**, 985 (2015).
 - [11] A. Aleman, H. Zaid, B. M. Cruz, K. Tanaka, J. M. Yang, H. Kindlund, and S. Kodambaka, *Acta Mater.* **221**, 117384 (2021).
 - [12] I. Mosyagin, D. Gambino, D. G. Sangiovanni, I. A. Abrikosov, and N. M. Caffrey, *Phys. Rev. B* **98**, 174103 (2018).
 - [13] D. G. Sangiovanni, F. Tasnadi, L. J. S. Johnson, M. Oden, and I. A. Abrikosov, *Phys. Rev. Mater.* **4**, 033605 (2020).
 - [14] R. F. Zhang, S. H. Zhang, Y. Q. Guo, Z. H. Fu, D. Legut, T. C. Germann, and S. Veprek, *Phys. Rep.* **826**, 1 (2019).
 - [15] J. Frenkel, *Z. Phys.* **37**, 572 (1926).
 - [16] W. Xu and J. A. Moriarty, *Phys. Rev. B* **54**, 6941 (1996).

- [17] A. T. Paxton, P. Gumbsch, and M. Methfessel, *Philos. Mag. Lett.* **63**, 267 (1991).
- [18] M. J. Mehl and L. L. Boyer, *Phys. Rev. B* **43**, 9498 (1991).
- [19] R. Miller and R. Phillips, *Philos. Mag. A* **73**, 803 (1996).
- [20] Y. Sun and E. Kaxiras, *Philos. Mag. A* **75**, 1117 (1997).
- [21] D. Roundy, C. R. Krenn, M. L. Cohen, and J. W. Morris, *Phys. Rev. Lett.* **82**, 2713 (1999).
- [22] S.-H. Jhi, S. G. Louie, M. L. Cohen, and J. W. Morris, *Phys. Rev. Lett.* **87**, 075503 (2001).
- [23] D. G. Sangiovanni, W. Mellor, T. Harrington, K. Kaufmann, and K. Vecchio, *Mater. Des.* **209**, 109932 (2021).
- [24] N. Koutná, L. Löfler, D. Holec, Z. Chen, Z. Zhang, L. Hultman, P. H. Mayrhofer, and D. G. Sangiovanni, *Acta Mater.* **229**, 117809 (2022).
- [25] A. B. Mei, H. Kindlund, E. Broitman, L. Hultman, I. Petrov, J. E. Greene, and D. G. Sangiovanni, *Acta Mater.* **192**, 78 (2020).
- [26] M. Yang and H. Sun, *Phys. Rev. B* **107**, 104101 (2023).
- [27] L. Wen, H. Wu, H. Sun, and C. Chen, *Carbon* **155**, 361 (2019).
- [28] H. Chacham and L. Kleinman, *Phys. Rev. Lett.* **85**, 4904 (2000).
- [29] D. Roundy and M. L. Cohen, *Phys. Rev. B* **64**, 212103 (2001).
- [30] Y. Zhang, H. Sun, and C. Chen, *Phys. Rev. B* **73**, 144115 (2006).
- [31] A. Nie, Y. Bu, J. Huang, Y. Shao, Y. Zhang, W. Hu, J. Liu, Y. Wang, B. Xu, Z. Liu *et al.*, *Matter* **2**, 1222 (2020).
- [32] B. Wang, *J. Appl. Mech.* **88**, 021008 (2020).
- [33] C. A. Schuh and A. C. Lund, *Nat. Mater.* **2**, 449 (2003).
- [34] A. C. Lund and C. A. Schuh, *Intermetallics* **12**, 1159 (2004).
- [35] M. Jahnátek, J. Hafner, and M. Krajčí, *Phys. Rev. B* **79**, 224103 (2009).
- [36] S. H. Zhang, Z. H. Fu, and R. F. Zhang, *Comput. Phys. Commun.* **238**, 244 (2019).
- [37] S. Ogata, J. Li, and S. Yip, *Science* **298**, 807 (2002).
- [38] J. F. Nye, *Physical Properties of Crystals: Their Representation by Tensors and Matrices* (Oxford University Press, Oxford, 1985).
- [39] G. E. Dieter and D. Bacon, *Mechanical Metallurgy* (McGraw-Hill, New York, 1986).
- [40] G. Kresse and D. Joubert, *Phys. Rev. B* **59**, 1758 (1999).
- [41] J. P. Perdew, K. Burke, and M. Ernzerhof, *Phys. Rev. Lett.* **77**, 3865 (1996).
- [42] G. Kresse and J. Furthmüller, *Phys. Rev. B* **54**, 11169 (1996).
- [43] G. Kresse and J. Furthmüller, *Comput. Mater. Sci.* **6**, 15 (1996).
- [44] See Supplemental Material at <http://link.aps.org/supplemental/10.1103/PhysRevB.107.224106> for initial atomic configurations of HfC and TaC along $[1\bar{1}0](110)$ and $[1\bar{1}0](111)$ direction; mechanical responses of HfC and TaC under pure shear and simple shear along $[\bar{1}\bar{1}2](111)$; and mechanical responses of HfC and TaC under semiconstrain shear.
- [45] D. J. Rowcliffe and W. J. Warren, *J. Mater. Sci.* **5**, 345 (1970).
- [46] T. Csanádi, E. Castle, M. J. Reece, and J. Dusza, *Sci. Rep.* **9**, 10200 (2019).
- [47] A. Kelly and D. J. Rowcliffe, *Phys. Status Solidi B* **14**, K29 (1966).
- [48] D. J. Rowcliffe and G. E. Hollox, *J. Mater. Sci.* **6**, 1270 (1971).
- [49] S. H. Zhang, D. Legut, and R. F. Zhang, *Comput. Phys. Commun.* **240**, 60 (2019).
- [50] C. Liu, X. Gu, K. Zhang, W. Zheng, Y. Ma, and C. Chen, *Phys. Rev. B* **105**, 024105 (2022).
- [51] B. Li, H. Sun, and C. Chen, *Phys. Rev. Lett.* **117**, 116103 (2016).
- [52] B. Li, H. Sun, and C. Chen, *Nat. Commun.* **5**, 4965 (2014).
- [53] W. Sun, X. Kuang, H. Liang, X. Xia, Z. Zhang, C. Lu, and A. Hermann, *Phys. Chem. Chem. Phys.* **22**, 5018 (2020).